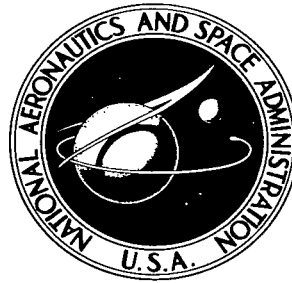NASA TECHNICAL NOTE

NASA TN D-4134
c.1

NASA TN D-4134

AERODYNAMIC INVESTIGATION OF SOME HIGH-DRAG ENTRY SHAPES AT MACH 15.4

by Frederick W. Gibson

Langley Research Center
Langley Station, Hampton, Va.

NASA TN D-4134

AERODYNAMIC INVESTIGATION OF SOME HIGH-DRAG

ENTRY SHAPES AT MACH 15.4

By Frederick W. Gibson

Langley Research Center
Langley Station, Hampton, Va.

NATIONAL AERONAUTICS AND SPACE ADMINISTRATION

AERODYNAMIC INVESTIGATION OF SOME HIGH-DRAG

ENTRY SHAPES AT MACH 15.4

By Frederick W. Gibson
Langley Research Center

SUMMARY

The effects of body shape, nose radius, and shoulder shape on separated flow, unsteady shocks, and aerodynamic drag for a series of 24 tension shell models at zero angle of attack and for a blunted 120° cone model at several angles of attack were investigated. The tests were conducted in helium flow at a Mach number of 15.4.

The results showed that certain tension shell configurations merit consideration for use as unmanned planetary entry vehicles because of the high drag coefficients (1.67 maximum). Model length and nose bluntness were found to affect flow separation, which is a major factor affecting the aerodynamic drag. The flow field on the tension shell is a complex one consisting of conical flow at the nose followed by isentropic compression up to a strong, nearly normal skirt shock. This shock is followed by a series of compressions and expansions with resulting pressure peaks and dips. The separated unsteady flow field on some tension shell models resulted in a lower drag coefficient, but the level of the pressure fluctuations was not determined. Data indicate that from high-drag considerations, an optimum shape can be found. The generally unpredictable aerodynamic characteristics of tension shells may offset the advantages of high drag and low structural weight. The experimental pressure distributions indicated that the Newtonian pressure distribution is only approximate for the tension shell shape. The pressure distribution for the blunted 120° cone model was substantially the same as that predicted by Newtonian theory. The level of pressure fluctuations on the surface of this model and the static pressure and fluctuating pressure levels behind this model were of the same order of magnitude as the free-stream static pressure.

INTRODUCTION

Of current interest is the suitability of several entry configurations for an unmanned Mars mission. One of the configurations that shows much promise is a so-called tension shell (ref. 1). Since this structure can be designed as a tension member, a low value of the ballistic coefficient can be obtained which is necessary in order to utilize the thin Martian atmosphere for braking the vehicle during entry.

Previous aerodynamic investigations (refs. 2 to 5) have indicated that such shapes may have extensive regions of separated flow and that there is a possibility of unsteady shocks on the body during entry. Therefore, the present investigation was undertaken to determine some of the effects of body fineness ratio, the ratio of nose radius to base radius, and the shape of the shoulder on the separated flow and unsteady shocks on a tension shell model at zero angle of attack. Twenty-four combinations of these parameters in the tension shell models were investigated. One blunted 120° cone model was tested at several angles of attack and the pressure distribution was determined on the vertical ray. High-speed schlieren motion pictures were obtained for all tests. Static pressures, fluctuating pressures, and aerodynamic drag were measured.

SYMBOLS

The units used for the physical quantities in this paper are given both in the U.S. Customary Units and in the International System of Units (SI). Conversion factors for the units used in the present investigation are presented in the appendix.

ⓐ,ⓑ,ⓒ,ⓓ	flow regions in figure 10
A^2	body shape parameter defined in reference 1
A_b	base area of model
C_D	drag coefficient, $\dfrac{\text{Drag}}{qA_b}$
$C_{p,max}$	maximum pressure coefficient
D	base diameter of model
F_X	axial force
l	length of model
M	free-stream Mach number
p	local static pressure
p_t	total pressure behind a normal shock

q   dynamic pressure

r   local body radius

r_b base radius

r_n nose radius

x   distance along axis of symmetry of model, measured from base of model (fig. 2)

α angle of attack

ρ density of medium

Subscripts:

1   conditions just upstream of normal shock

2   conditions just downstream of normal shock

APPARATUS

The tests were conducted in the 24-inch-diameter (60.96-cm) nozzle of the Langley hypersonic aeroelasticity tunnel. This is a blowdown-type tunnel which operates at an average test-section Mach number of 15.4 and which uses helium as a test medium. A description of this apparatus is given in reference 6. For the present tests, the stagnation pressures ranged from 700 to 1000 psia $\left(4.8 \text{ to } 6.9 \text{ MN}/\text{m}^2\right)$, the stagnation temperatures ranged from 70° to 80° F (294° to 300° K), and the Reynolds numbers ranged from approximately 5×10^6 to 7×10^6 per foot (16.40 to 22.96 per μm).

MODELS AND INSTRUMENTATION

Tension Shell Models

The tension shell is a shell of revolution designed to have only tensile stresses under axisymmetric loadings. A complete description and derivation is given in reference 1. In the present investigation, 24 tension shell models were tested. The variable body parameters for the models used were body shape, nose radius, and shoulder shape. The orientation of the model axes and force reference axes is shown in figure 1. The

general dimensions of the three body shapes, the details of the shoulder shapes, and the nose radii are shown in figure 2. Table I presents the external surface coordinates and the locations of the pressure orifices. The three model body shapes were designated by the parameters $A^2 = 1.27$, $A^2 = 1.4$, and $A^2 = 1.6$. Each model had a base radius of 1.5 inches (3.81 cm). The ratios of nose radius to base radius (r_n/r_b) were 0, 0.05, and 0.10, and these were designated sharp, medium, and blunt, respectively. The shoulder shapes were called round, square, and sharp (see fig. 2).

For the static-pressure survey, all tests except one used a row of five orifices located along a ray of the model. For the exception noted, 10 additional orifices were located in the model with $A^2 = 1.4$, $r_n/r_b = 0$, and the round shoulder. The locations of these orifices are given in table I and identified with an asterisk. For the fluctuating-pressure survey, five orifices were located in a similar array oriented 180° radially from the static-pressure orifices. The miniature gages used to measure fluctuating pressures were mounted as close to the surface as was practicable.

Blunted Cone Model

One blunted 120° cone model was tested. The model is shown in figure 3. The base diameter was 3 inches (7.62 cm) and the nose radius was 25 percent of the base radius. Orifice locations and dimensions are given in figure 3.

Instrumentation and Equipment

All models were sting mounted and a strain-gage balance was used to measure axial force; however, the blunted cone model was tested without a force balance. In addition to the aforementioned pressure gages which were used to measure the static and fluctuating pressures on the surface of the models, one pressure gage was mounted behind the model to check for fluctuating pressure downstream of and close to the base of the model.

An oscillograph was used to record the outputs of the static-pressure gages, accelerometers, and strain-gage balance. The fluctuating-pressure data were recorded on magnetic tape.

Photographs of the flow fields were obtained for all tests. A single-pass schlieren system and a high-speed 16-mm motion-picture camera with a framing speed of approximately 2800 frames per second were used. A mercury-arc light with dc power supply was used for a light source.

TEST PROCEDURES AND DATA REDUCTION

All tests on the tension shell models were conducted with the model mounted in the center of the test section at zero angle of attack. A protective metal cone was in front of

the model until flow was established, retracted into a recess in the tunnel wall for the desired interval, and then returned to protect the model during tunnel shutdown. The blunted 120° cone model was mounted in the center of the tunnel at the desired angle of attack. A paper cone was in front of the model until flow was established and then pulled off and discarded in the flow. Since no force balance was used with this model, no protection was needed during tunnel shutdown.

Schlieren Photographs

Schlieren motion pictures were obtained for each run. The film and the oscillograph record were time correlated from motion of the protective cone, and the frames shown in figure 4 are for maximum-stagnation-pressure tunnel conditions.

Static-Pressure Distributions

Variable-reluctance-type pressure gages were used to measure the static pressures on the surface of the model and in the shadow of the model. These gages were calibrated before each run. The pressure data refer to the time the tunnel was at maximum stagnation pressure. The static pressures were nondimensionalized by dividing them by the theoretical total pressure behind the normal shock. These pressure gages had response characteristics which were flat with frequency up to about 2000 cps; however, the recording system was only flat to 600 cps.

Fluctuating Pressures

The fluctuating pressures were recorded on the magnetic tape along with appropriate calibration data. The tapes were analyzed for power spectral density and mean-square pressure fluctuations. The natural frequency of the miniature gages used for this phase was 60 000 cps and the recording system was flat to 3000 cps.

Theoretical Calculations

The data generated in this investigation have been compared with results obtained by Newtonian theory. The theoretical values were calculated by using a modified value of $C_{p,max}$ of 1.765 which was derived by inserting the perfect-gas values from the tables of reference 7 into the equation for the pressure coefficient behind a normal shock.

RESULTS AND DISCUSSION

Tension Shell Models

Schlieren data.- Schlieren photographs of 24 tension shell configurations are shown in figure 4. For the model configurations on which the shocks were steady, only one

frame is shown. For those models on which the shocks were unsteady, two or more frames are shown to illustrate the changing shock patterns (except for the model with $A^2 = 1.6$, $r_n/r_b = 0.10$, and the square shoulder for which only one photograph was available). No consistent effect of increasing stagnation pressure, and hence Reynolds number, could be observed in the motion pictures. The results of an investigation reported in reference 4, however, indicate that increasing Reynolds number reduces the extent of separation and stabilizes the flow on some body shapes but has the opposite effect on other shapes. The data for the present tests show that model length and nose bluntness affect flow separation, which is a major factor affecting aerodynamic drag. A study of the results as presented in table II indicates that the flow was unsteady on all model configurations having the largest fineness ratio $(A^2 = 1.6)$. Also, table II shows that on the two models with larger fineness ratios (i.e., $A^2 = 1.4$ and $A^2 = 1.6$), the shape of the shoulder is a major factor contributing to the unsteady flow. Specifically, the models with square shoulders are completely unsteady, whereas the round-shoulder models had either completely steady flow or only intermittent bursts of unsteady flow. Decreasing the fineness ratio has a stabilizing effect. Increasing nose bluntness appears to be destabilizing.

Drag data.- A summary of the drag data is presented in figure 5 where C_D is plotted as a function of fineness ratio. The data show a general trend of decreasing drag coefficient with increasing fineness ratio, although the drag coefficient of the sharp-nose models remains relatively unchanged with increasing fineness ratio except for the models with sharp nose and sharp shoulder. For these models, the value of C_D shows a large increase, to a maximum of 1.67, as the fineness ratio increased from $l/r_b = 1.0$ to $l/r_b = 1.16$; with further increase in fineness ratio to $l/r_b = 1.41$, the value of C_D shows a large decrease. The normal tendency to view such variant data with suspicion must be subdued in this case because of the extreme complexity of the flow field on the tension shell models. The data of figure 5 indicate that an optimum shape for high drag can be found.

Pressure distributions.- The pressure distributions for the tension shell models are presented in figures 6 to 9. Figures 6, 7, and 8 are for models $A^2 = 1.27$, $A^2 = 1.4$, and $A^2 = 1.6$, respectively. The need for additional orifices to define the pressure distribution more accurately is evident from these figures. Therefore, the model with $A^2 = 1.4$, $r_n/r_b = 0$, and the round shoulder was tested with 10 additional orifice locations and the data are presented in figure 9. Also plotted in figure 9 are theoretical curves from references 4 and 8 and the pressure distribution predicted by Newtonian theory. The highest experimental pressure is seen to be approximately 1.4 times the total pressure behind the normal shock. In the investigation reported in reference 4, pressures as high as 2.2 times the normal-shock total pressure were measured. According to the flow-field analysis presented in references 4 and 8, the first pressure peak occurs just aft of the

6

shock intersection. Figure 9, therefore, serves to illustrate the dependence of the first pressure peak on the normal-shock density ratio. The figure shows that the pressure-peak location is moving rearward on the model as the shock density ratio increases. For the convenience of the reader, a sketch of the flow field on a tension shell is presented in figure 10. The following explanation of this flow field is a condensed version of the one given in reference 4. On the nose portion, the flow is conical and then turns isentropically until it meets the skirt shock. Behind the skirt shock, region ©, is a subsonic constant-pressure region. The fact that this region must remain at constant pressure imposes a constant-pressure boundary on the lower entropy region along the model surface $\left(\text{regions } \text{ⓐ}, \text{ⓑ}, \text{ and } \text{ⓓ}\right)$. These regions remain supersonic. This constant-pressure boundary is a slip flow line or vortex sheet. The flow in region ⓐ turns to produce a pressure increase to the level prevailing in region ©; therefore, an oblique shock is formed between regions ⓐ and ⓑ. This shock reflects from the model surface and impinges on the slip flow line where it must expand to reach a static pressure again equal to that in region ©. The pressure behind the reflected shock $\left(\text{region } \text{ⓓ}\right)$ is very high. The pressure at the point where the expansion fan intersects the model surface is very low. The flow, therefore, between the body surface and the vortex sheet is characterized by a series of reflected shocks and expansions with consequently widely varying surface pressures. A close inspection of some of the schlieren photographs of figure 4 reveals some areas near the body aft of the skirt shock that appear to be expansion and compression areas. Another photograph which more clearly shows these compressions and expansions (from ref. 4) is reproduced in figure 10 with the sketch of the theoretical flow field.

The static pressures behind the tension shell model were of the same order of magnitude as the free-stream static pressure and ranged from approximately 0.010 to 0.020 psia $\left(68.95 \text{ to } 137.90 \text{ N/m}^2\right)$.

Fluctuating Pressures

Although the steady surface pressure distribution had many peaks (as seen in fig. 9), the root-mean-square level of the unsteady pressure fluctuations on the surface of and behind the tension shell models was less than 0.1 psia $\left(689.48 \text{ N/m}^2\right)$. The sensitivity of the recorder used in the analysis is such that readings in this range are unreliable; therefore, the data are not presented.

Blunted Cone Model

The pressure-distribution data for the blunted 120° cone model are presented in figure 11. Newtonian theory gives an average value of the measured pressures. The level of pressure behind the model was of the same order of magnitude as free-stream

static pressure and ranged from approximately 0.010 to 0.020 psia $\left(68.95 \text{ to } 137.90 \text{ N/m}^2\right)$. No fluctuating pressures could be observed.

CONCLUSIONS

The effects of body shape, nose radius, and shoulder shape on static pressures, aerodynamic drag, and shock patterns for a series of 24 tension shell shapes and for a blunted 120° cone were investigated. Based on the results, the following conclusions were drawn:

1. Certain tension shell configurations merit consideration for use as unmanned planetary entry vehicles because of the high drag coefficients measured (1.67 maximum); however, their generally unpredictable aerodynamic characteristics may offset the obvious advantages of high drag and low structural weight.

2. Model length and nose bluntness affect flow separation, which is a major factor affecting the aerodynamic drag.

3. The unsteady flow field and associated flow separation on the tension shell model with the largest fineness ratio resulted in a lower drag coefficient than was found on the shorter models. The data indicate that an optimum shape for high drag can be found.

4. Unsteady flow fields occur on some tension shell shapes; however, the level of pressure fluctuations was not determined.

5. The shape of the shoulder on the tension shell models affects the flow field. The square-shoulder shape seems to be destabilizing, whereas the round-shoulder and sharp-shoulder shapes had no consistent effect.

6. The pressure distribution on the blunted 120° cone model was substantially the same as that predicted by Newtonian theory. The level of pressure fluctuations on the surface of the model and the static pressure and fluctuating pressure levels behind the model were of the same order of magnitude as the free-stream static pressure.

Langley Research Center,
    National Aeronautics and Space Administration,
        Langley Station, Hampton, Va., March 8, 1967,
            124-08-05-10-23.

APPENDIX

CONVERSION OF U.S. CUSTOMARY UNITS TO INTERNATIONAL
SYSTEM OF UNITS (SI)

Factors required for converting the U.S. Customary Units used herein to the International System of Units (SI) are given in the following table:

Physical quantity	U.S. Customary Unit	Conversion factor (*)	SI Unit (**)
Length	in.	0.0254	meters (m)
Pressure	psia $= lbf/in^2$	6895	newtons/meter^2 $\left(N/m^2\right)$
Temperature . . .	°F	$\frac{5}{9}(F + 459.67)$	degrees Kelvin (°K)

*Multiply the value given in U.S. Customary Units by the conversion factor to obtain the equivalent value in SI Units.

**Prefixes to indicate multiple of units are as follows:

Prefix	Multiple
mega (M)	10^6
centi (c)	10^{-2}
micro (μ)	10^{-6}

REFERENCES

1. Anderson, Melvin S.; Robinson, James C.; Bush, Harold G.; and Fralich, Robert W.: A Tension Shell Structure for Application to Entry Vehicles. NASA TN D-2675, 1965.

2. Bernot, Peter T.: Longitudinal Stability Characteristics of Several Proposed Planetary Entry Vehicles at Mach 6.73. NASA TN D-2785, 1965.

3. Robinson, James C.; and Jordan, Alfred W.: Exploratory Experimental Aerodynamic Investigation of Tension Shell Shapes at Mach 7. NASA TN D-2994, 1965.

4. Jones, Robert A.; Bushnell, Dennis M.; and Hunt, James L.: Experimental Flow Field and Heat-Transfer Investigation of Several Tension Shell Configurations at a Mach Number of 8. NASA TN D-3800, 1967.

5. Deveikis, William D.; and Sawyer, James Wayne: Aerodynamic Characteristics of Tension Shell Shapes at Mach 3.0. NASA TN D-3633, 1966.

6. Goetz, Robert C.: Effects of Leading-Edge Bluntness on Flutter Characteristics of Some Square-Planform Double-Wedge Airfoils at a Mach Number of 15.4. NASA TN D-1487, 1962.

7. Mueller, James N.: Equations, Tables, and Figures for Use in the Analysis of Helium Flow at Supersonic and Hypersonic Speeds. NACA TN 4063, 1957.

8. Anon.: Comparative Studies of Conceptual Design and Qualification Procedures for a Mars Probe/Lander. Volume V: Subsystem and Technical Analyses – Book 2: Aeromechanics and Thermal Control. AVSSD-0006-66-RR (Contract NAS 1-5224), AVCO Corp., May 11, 1966.

TABLE I.- SURFACE COORDINATES AND PRESSURE ORIFICE LOCATIONS OF TENSION SHELL MODELS

	Surface coordinates				Pressure orifice locations		
	x/r_b for –				r/r_b for –		
r/r_b	$A^2 = 1.27$	$A^2 = 1.4$	$A^2 = 1.6$		$A^2 = 1.27$	$A^2 = 1.4$	$A^2 = 1.6$
0	1.00	1.160	1.413		0.36	*0.29	0.36
.05	.918	1.065	1.294		.444	*.33	.455
.10	.839	.970	1.177		.57	.35	.543
.15	.760	.877	1.061		.704	*.37	.666
.20	.683	.787	.949		.789	*.416	.75
.25	.608	.699	.840			.447	
.30	.536	.615	.736			*.46	
.35	.467	.534	.637			*.51	
.40	.404	.459	.545			.547	
.45	.341	.388	.459			*.563	
.50	.284	.322	.380			*.618	
.55	.232	.263	.308			.663	
.60	.185	.209	.243			*.683	
.65	.143	.161	.187			*.751	
.70	.106	.119	.137			.78	
.75	.074	.083	.096				
.80	.048	.053	.062				
.85	.027	.030	.035				
.90	.012	.014	.016				
.95	.004	.003	.004				
1.00	0	0	0				

*Used for one test only.

TABLE II.- SUMMARY OF THE DATA SHOWING THE EFFECT OF THE BODY PARAMETERS
ON THE STABILITY OF THE FLOW FIELD

Model shape parameter, A^2	Model fineness ratio, l/r_b	Shoulder shape	Nose shape	Flow field*	
				Steady	Unsteady
1.6	1.413	Round	Sharp	▮	▮
		Round	Medium	▮	▮
		Sharp	Sharp		▮
		Sharp	Medium		▮
		Sharp	Blunt	▮	▮
		Square	Sharp		▮
		Square	Medium		▮
		Square	Blunt		▮
1.4	1.16	Round	Sharp	▮	
		Round	Medium	▮	
		Sharp	Sharp	▮	
		Sharp	Medium		▮
		Sharp	Blunt		▮
		Square	Sharp		▮
		Square	Blunt		▮
1.27	1.00	Round	Sharp	▮	
		Round	Medium	▮	
		Round	Blunt		▮
		Sharp	Sharp	▮	
		Sharp	Medium	▮	
		Sharp	Blunt		▮
		Square	Sharp	▮	
		Square	Medium	▮	
		Square	Blunt		▮

*Half-bar symbols ▬ signify steady flow with intermittent bursts of unsteady flow; long-bar symbols ▮ signify completely steady or unsteady flow.

12
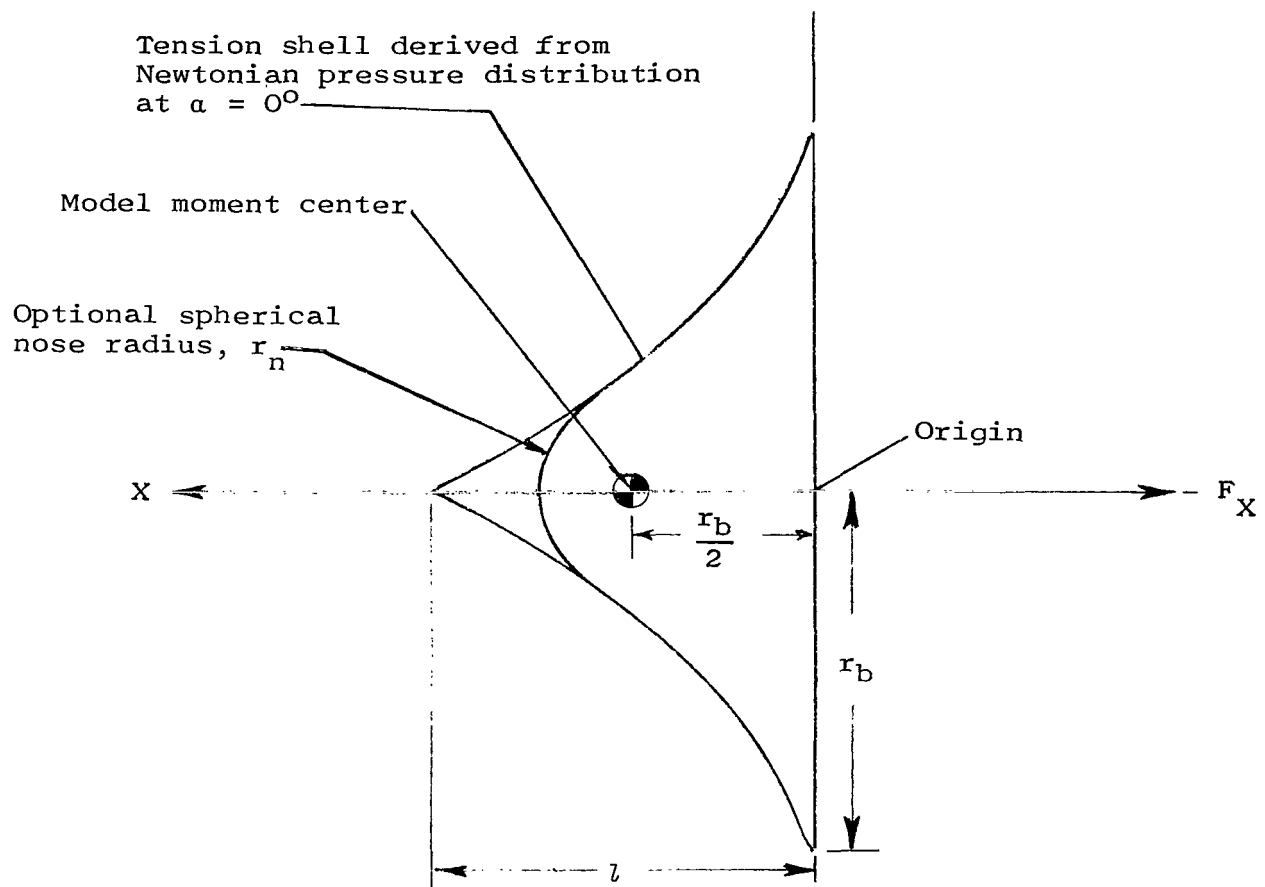
Figure 1.- Sketch indicating the orientation of model axes and force reference axes.

$r_n \, / \, r_b =$

0.10
0.05
0

Details 'A'

r

x

D

l

Radius = $0.08\,r_b$

Round shoulder

0.0832 r_b

Square shoulder

30°

Sharp shoulder

Details 'A'

Orifice
0.020 in.
(0.05 cm)

Model surface

0.020 in.
(0.05 cm)

Miniature gage

Sketch of miniature-
pressure-gage mounting

Model
surface

Sketch of static-
pressure orifice
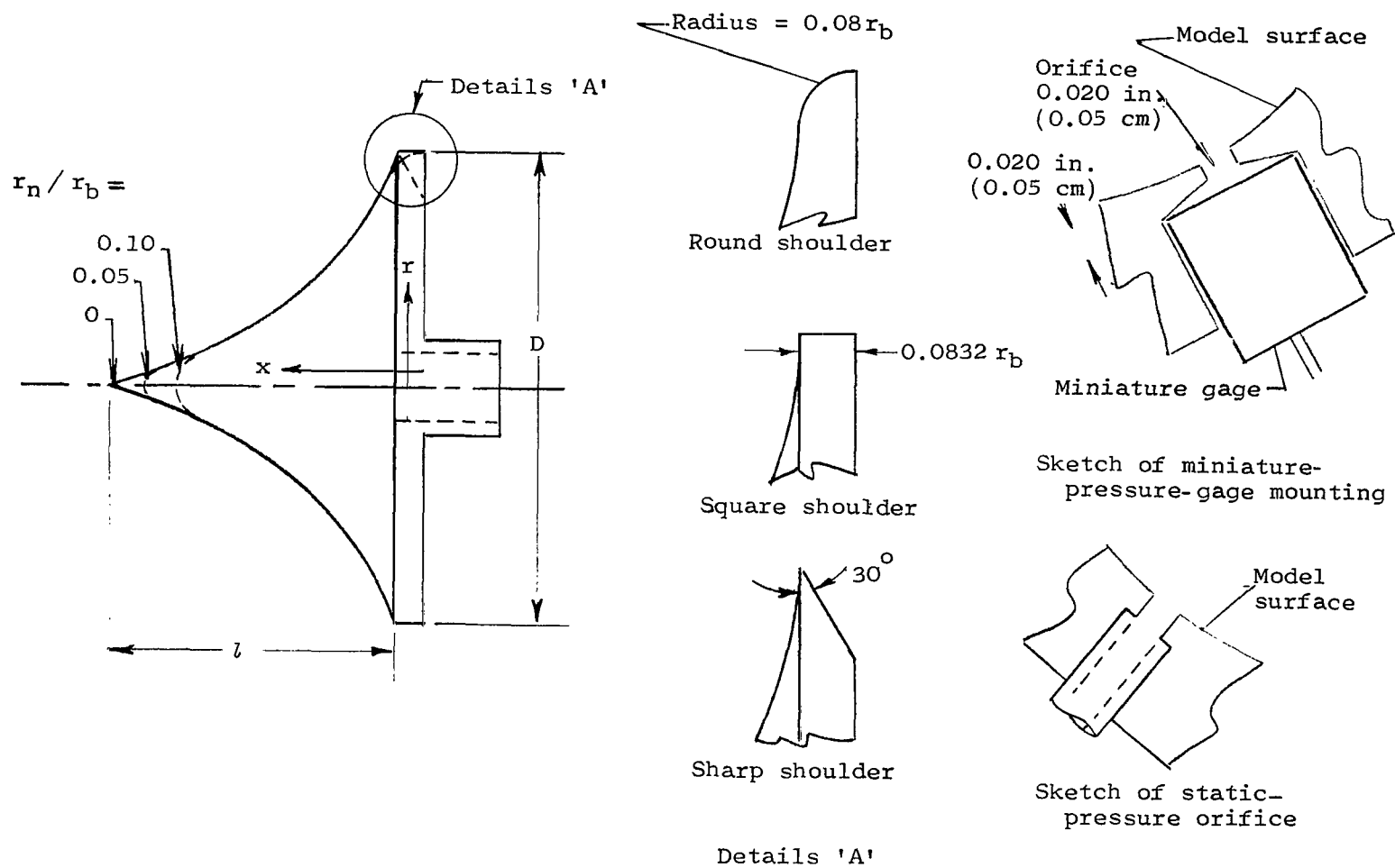
Figure 2.- Sketch of the tension shell models showing the general dimensions and the nose and shoulder shapes.

Radius = $0.08\, r_b$
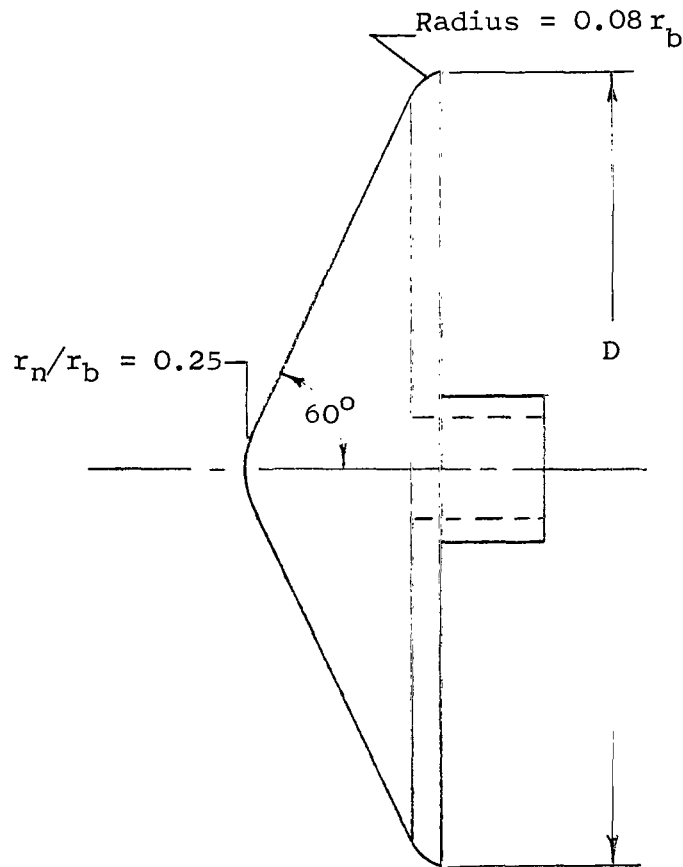
Orifice locations
on model surface

r/r_b

0.187
.280
.465
.643
.822

$r_n/r_b = 0.25$

60°

D
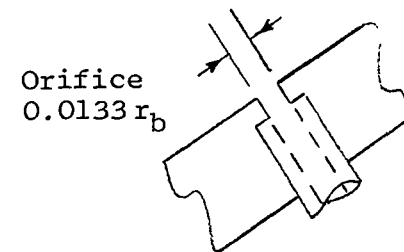
Orifice
$0.0133\, r_b$

Sketch of pressure orifice

Figure 3.- Sketch of the blunted 120° cone model.

$r_n/r_b = 0$
Steady
Round shoulder

$r_n/r_b = 0.05$
Steady
Round shoulder

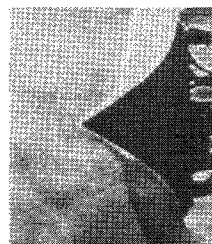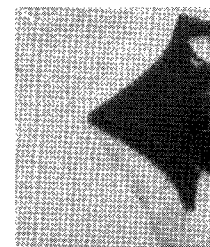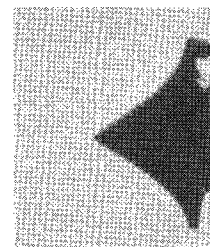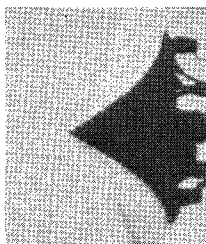$r_n/r_b = 0.05$
Unsteady
Square shoulder

$r_n/r_b = 0$
Unsteady
Sharp shoulder

$r_n/r_b = 0.05$
Unsteady
Sharp shoulder

$r_n/r_b = 0.10$
Steady
Sharp shoulder

$r_n/r_b = 0$
Unsteady
Square shoulder

$r_n/r_b = 0.10$
Unsteady
Square shoulder
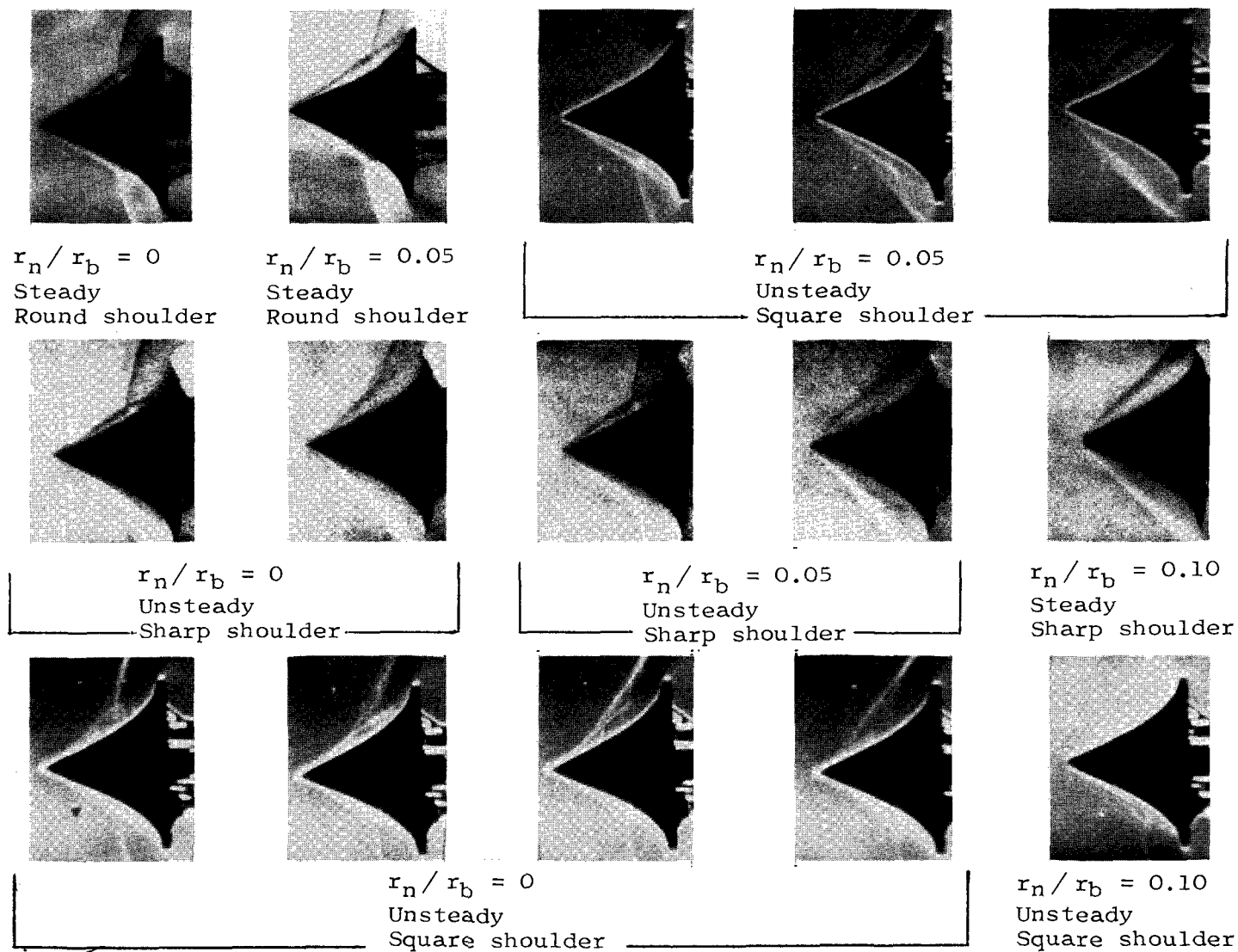
(a) $A^2 = 1.6$.

L-67-1051

Figure 4.-   Schlieren photographs of the tension shell model showing some effects of nose bluntness, shoulder shape, and body fineness ratio on the shock shape.

$$r_n / r_b = 0.05$$
Unsteady
Round shoulder

$r_n / r_b = 0$
Steady
Round shoulder

$$r_n / r_b = 0.10$$
Unsteady
Square shoulder

$$r_n / r_b = 0.10$$
Unsteady
Sharp shoulder

$r_n / r_b = 0$
Steady
Sharp shoulder

$$r_n / r_b = 0.05$$
Unsteady
Sharp shoulder
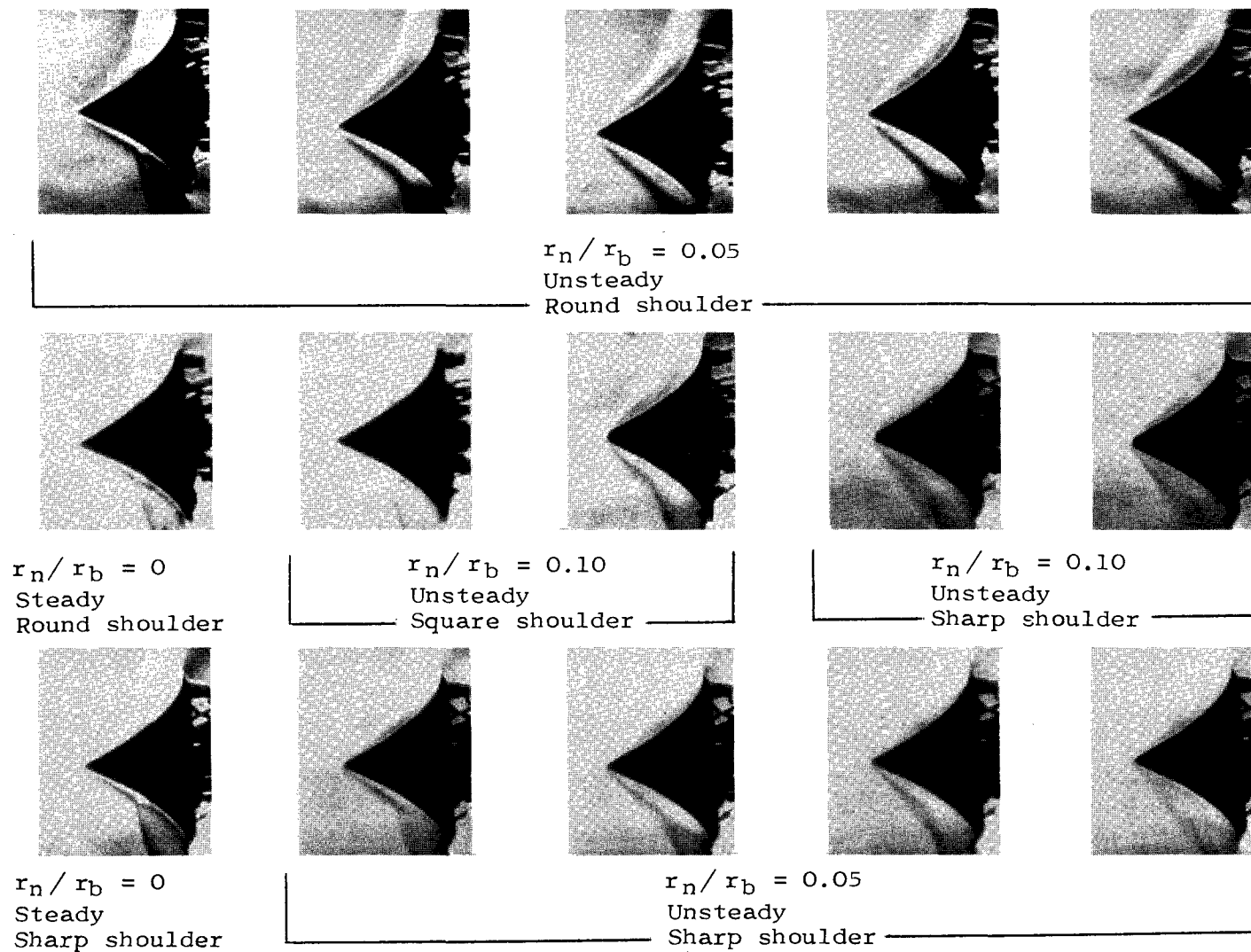
(b) $A^2 = 1.4$.

L-67-1052

Figure 4.- Continued.
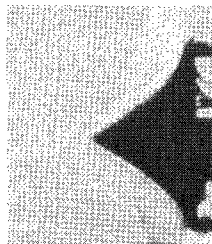
$r_n / r_b = 0$
Steady
Round shoulder

$r_n / r_b = 0.05$
Steady
Round shoulder
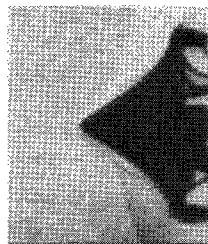
$r_n / r_b = 0.10$
Unsteady
Round shoulder
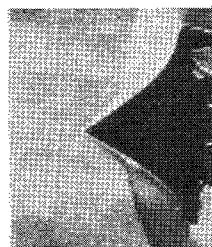
$r_n / r_b = 0$
Steady
Square shoulder

$r_n / r_b = 0.05$
Steady
Square shoulder
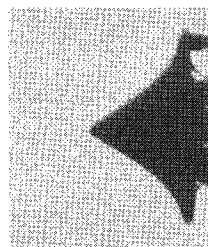
$r_n / r_b = 0.10$
Unsteady
Square shoulder

$r_n / r_b = 0$
Steady
Sharp shoulder

$r_n / r_b = 0.05$
Steady
Sharp shoulder
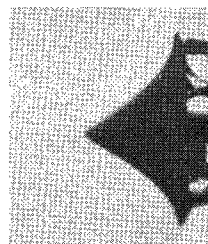
$r_n / r_b = 0.10$
Unsteady
Sharp shoulder
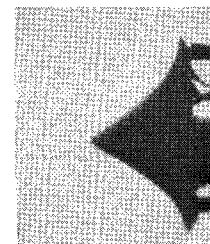
(c) $A^2 = 1.27$.
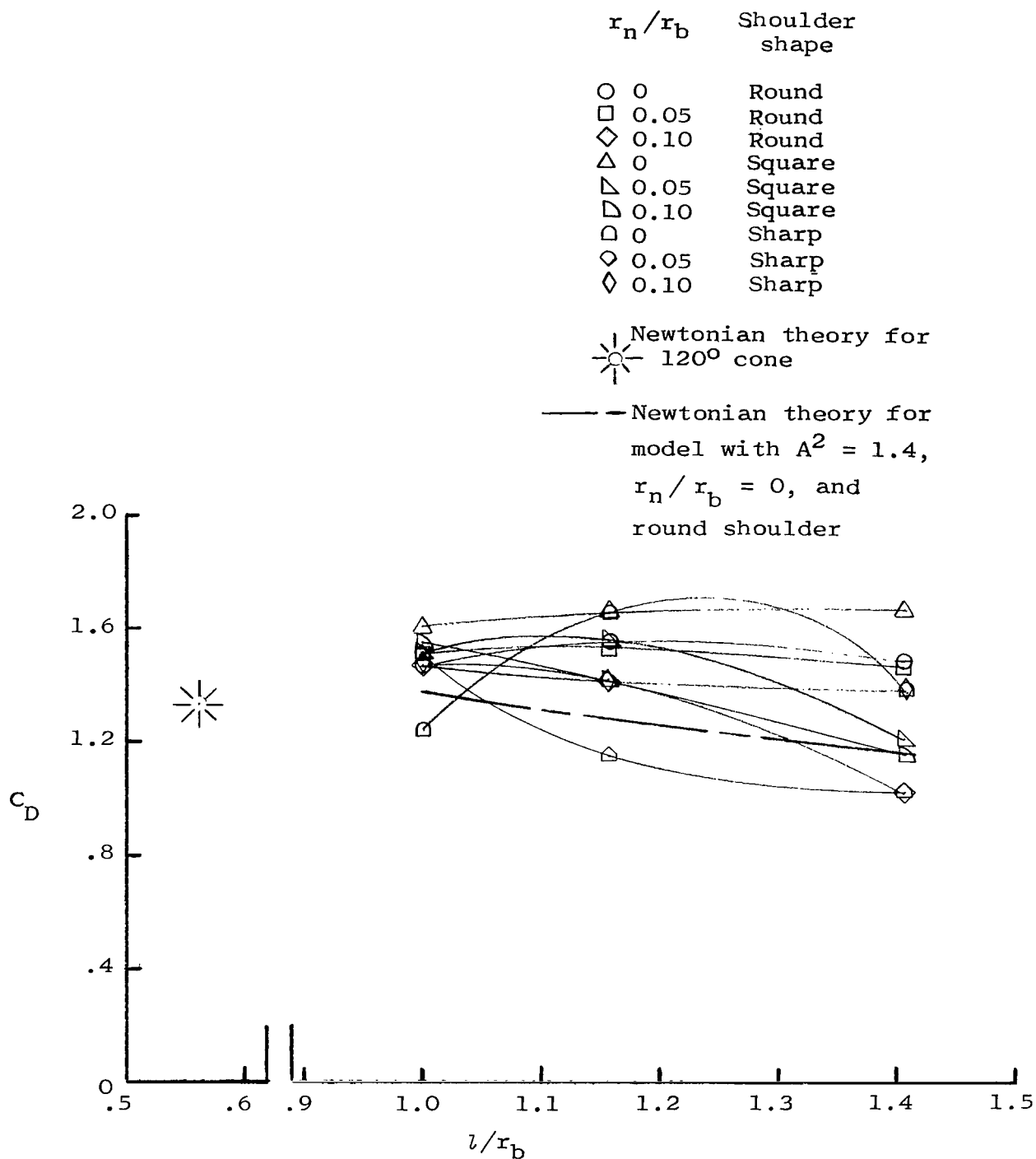
Figure 4.- Concluded.

L-67-1053

Figure 5.- Variation of drag coefficient with fineness ratio for the tension shell shapes showing some effects of nose bluntness and shoulder shape.
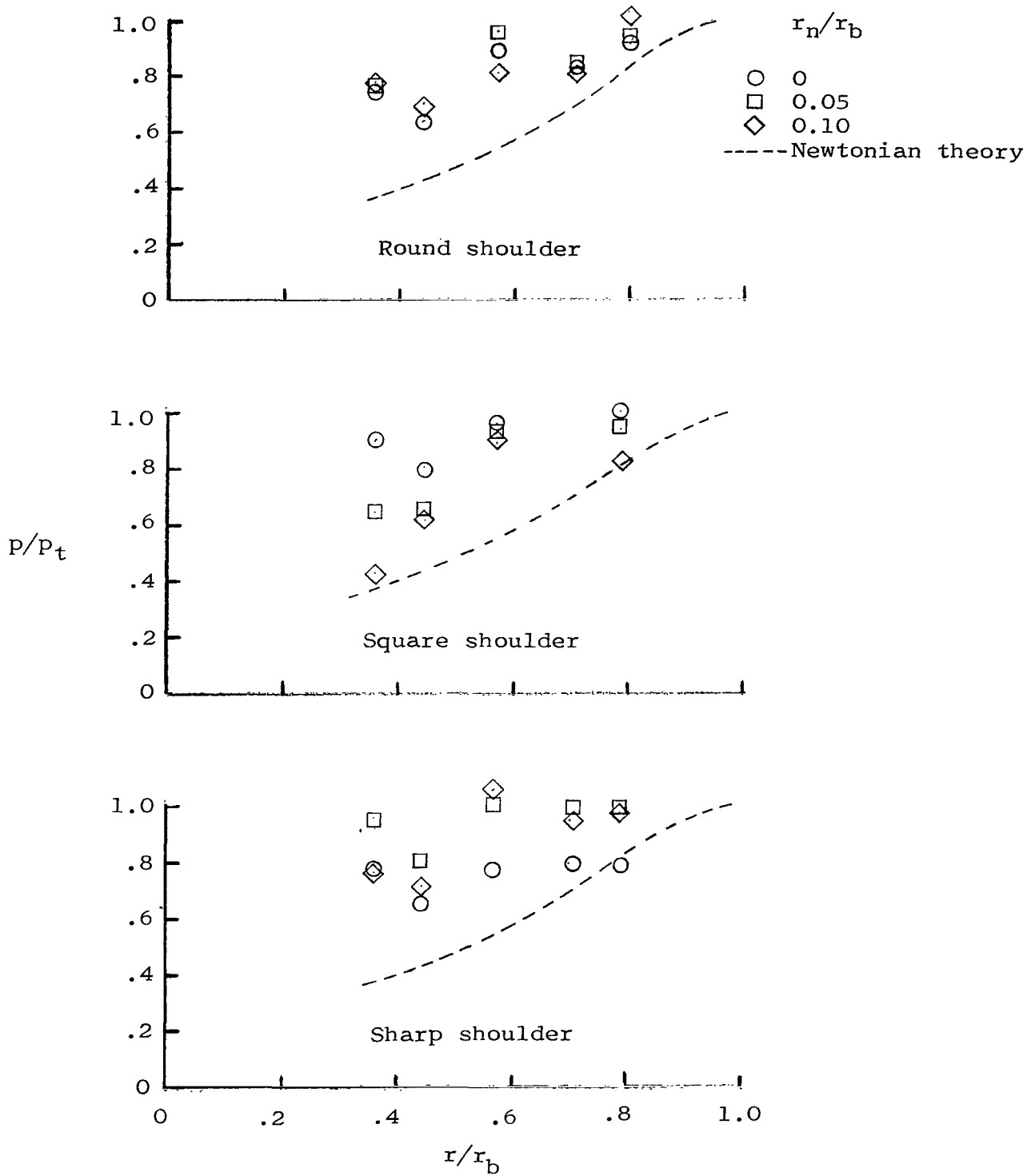
Figure 6.- Pressure distribution on tension shell model $A^2 = 1.27$ showing the effects of nose bluntness and shoulder shape. $M = 15.4$; $\alpha = 0^{\circ}$.
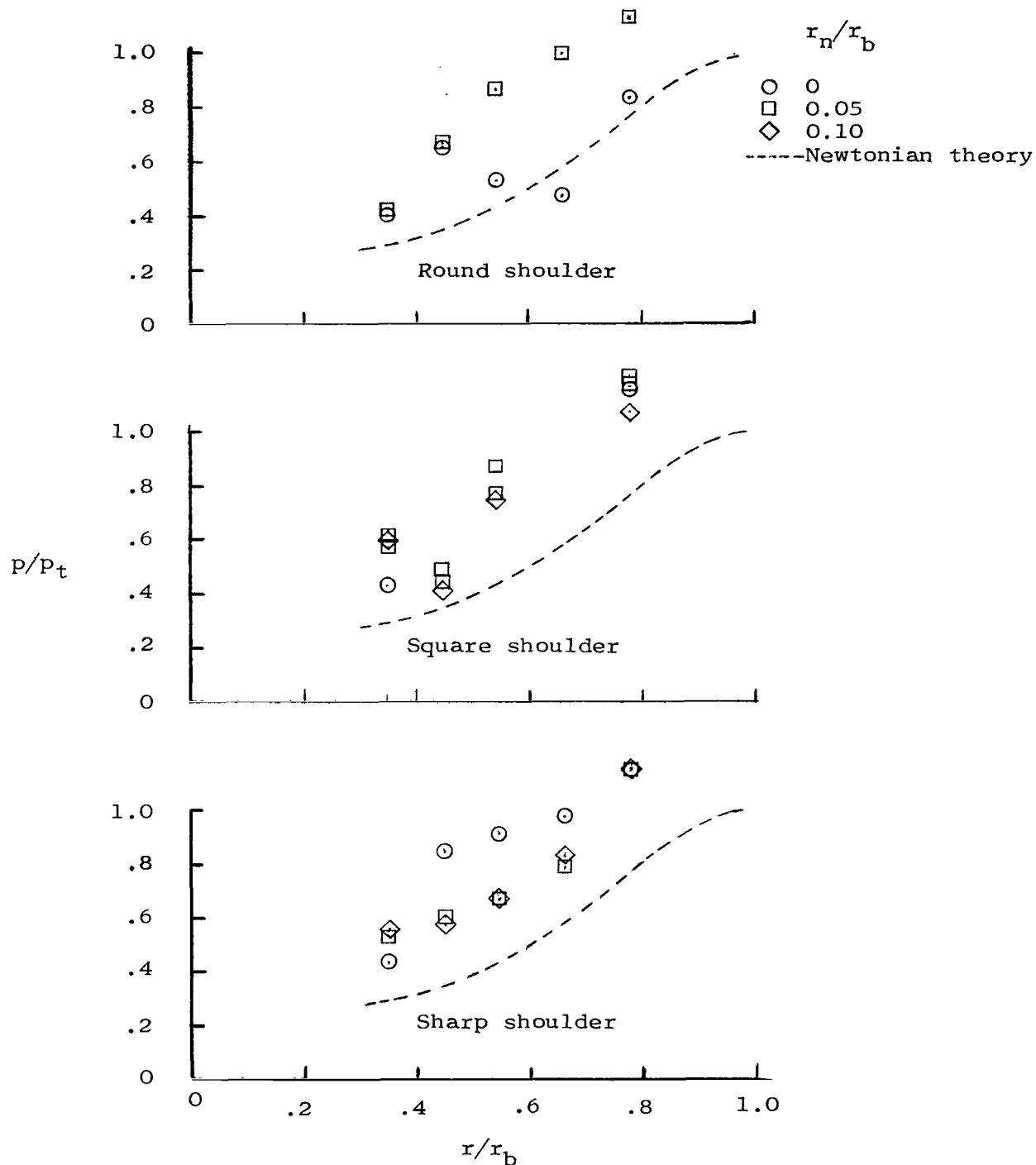
Figure 7.- Pressure distribution on tension shell model $A^2 = 1.4$ showing the effects of nose bluntness and shoulder shape. $M = 15.4$; $\alpha = 0^o$.
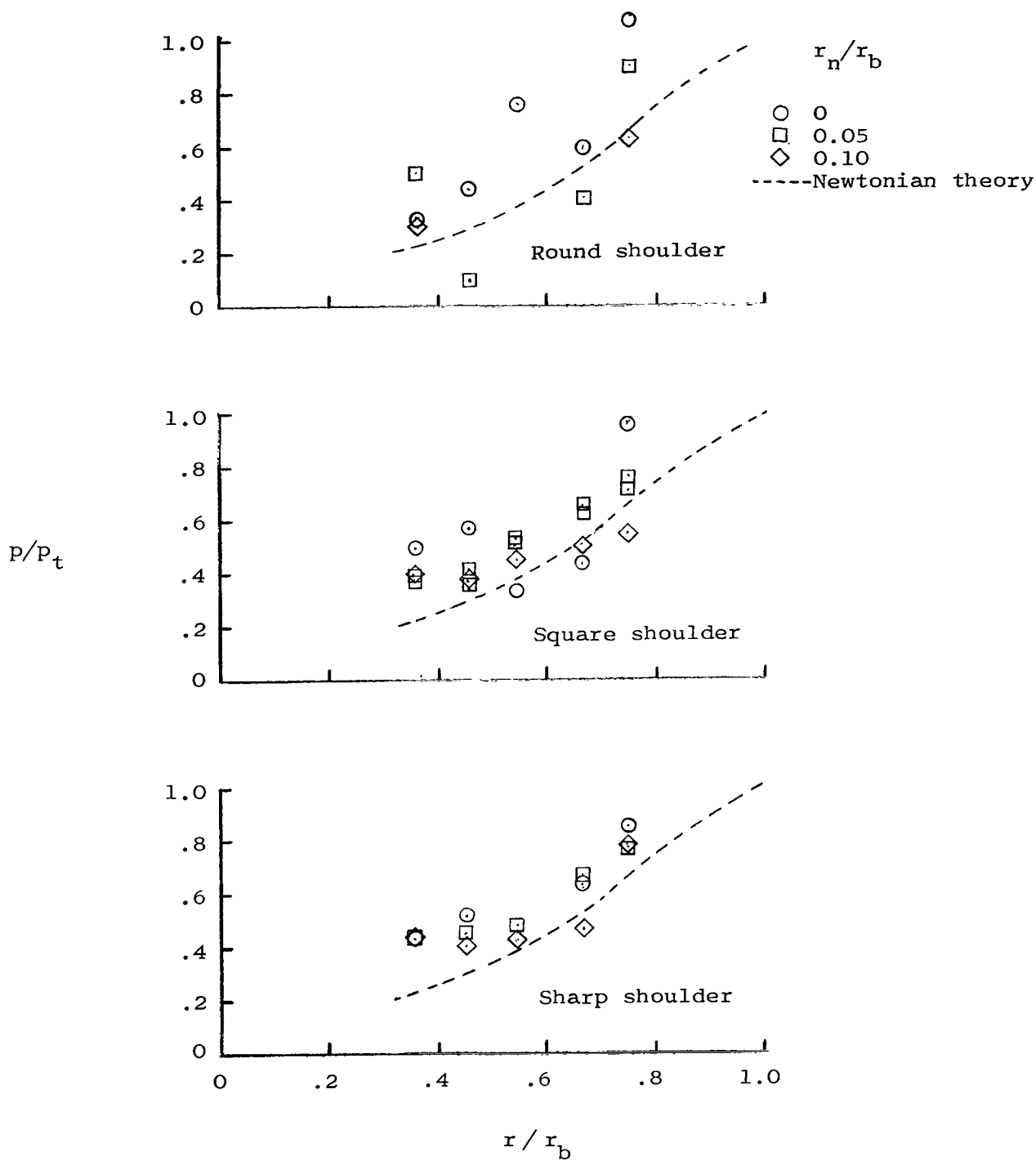
Figure 8.- Pressure distribution on tension shell model $A^2 = 1.6$ showing the effects of nose bluntness and shoulder shape. $M = 15.4$; $\alpha = 0^0$.
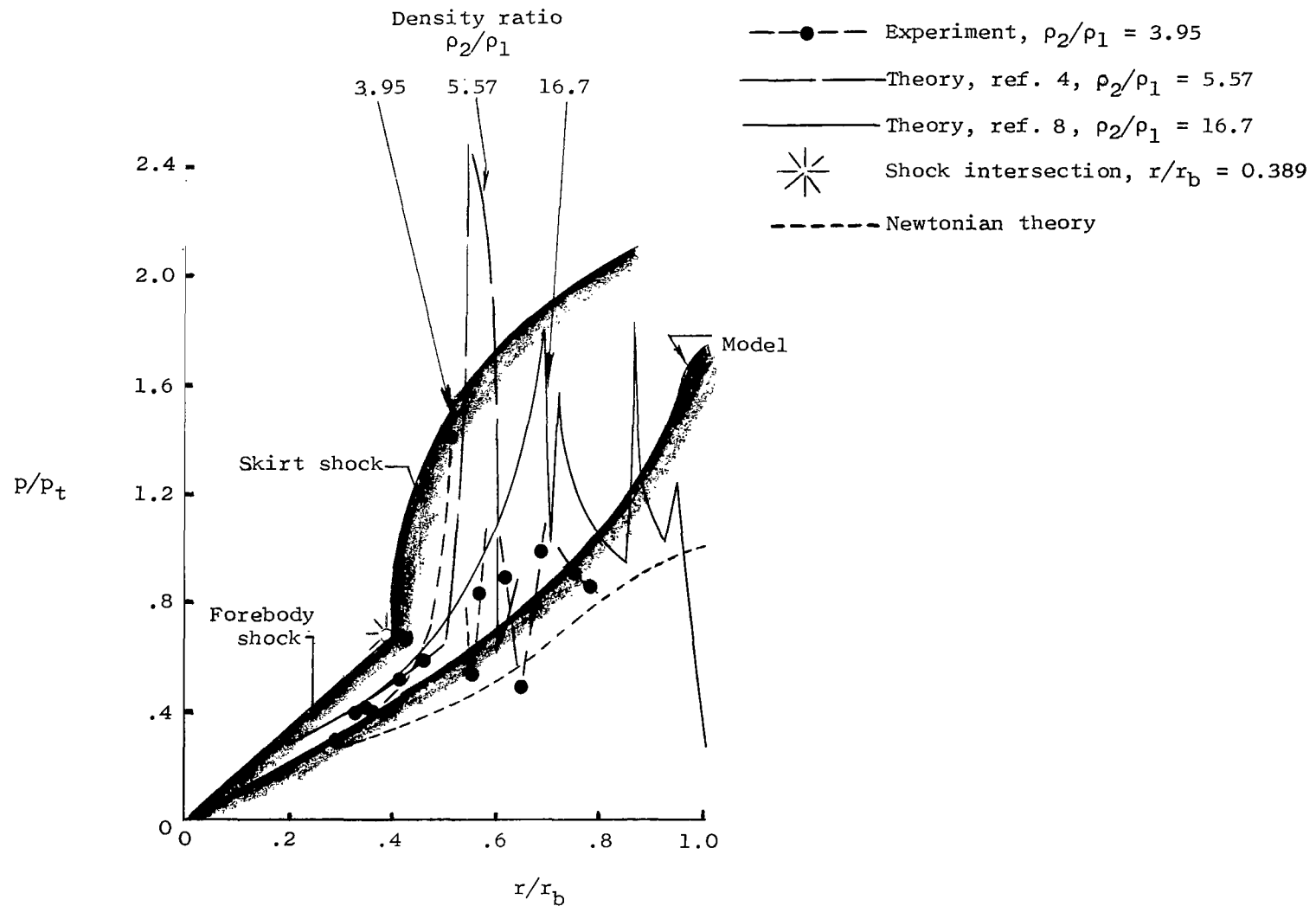
Figure 9.- Comparison of calculated and measured pressure distributions on a tension shell model $\left(A^2 = 1.4, \quad r_n/r_b = 0, \text{ and round shoulder}\right)$ showing effects of the normal-shock density ratio.
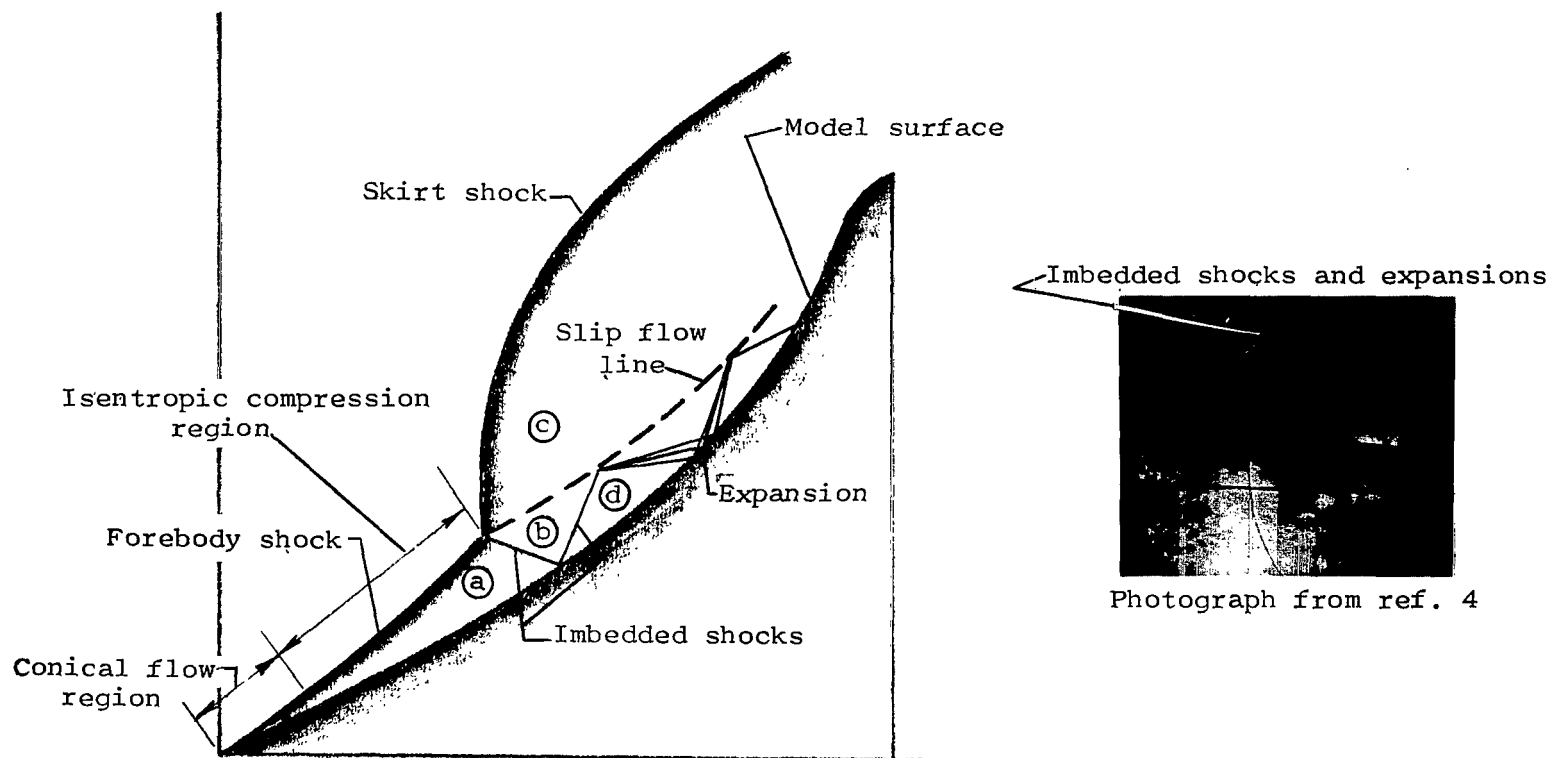
Figure 10.- Sketch of theoretical flow field.

L-66-7619

-------- Newtonian theory

1.0

.8

.6

.4

.2

0

$\alpha = 0^o$

$\alpha = -6^o$

P/P_t

1.0

.8

.6

.4

.2

0

$\alpha = 6^o$

$\alpha = -18^o$

0   .2   .4   .6   .8   1.0

r/r_b

1.0

.8

.6

.4

.2

0

$\alpha = 12^o$

0   .2   .4   .6   .8   1.0

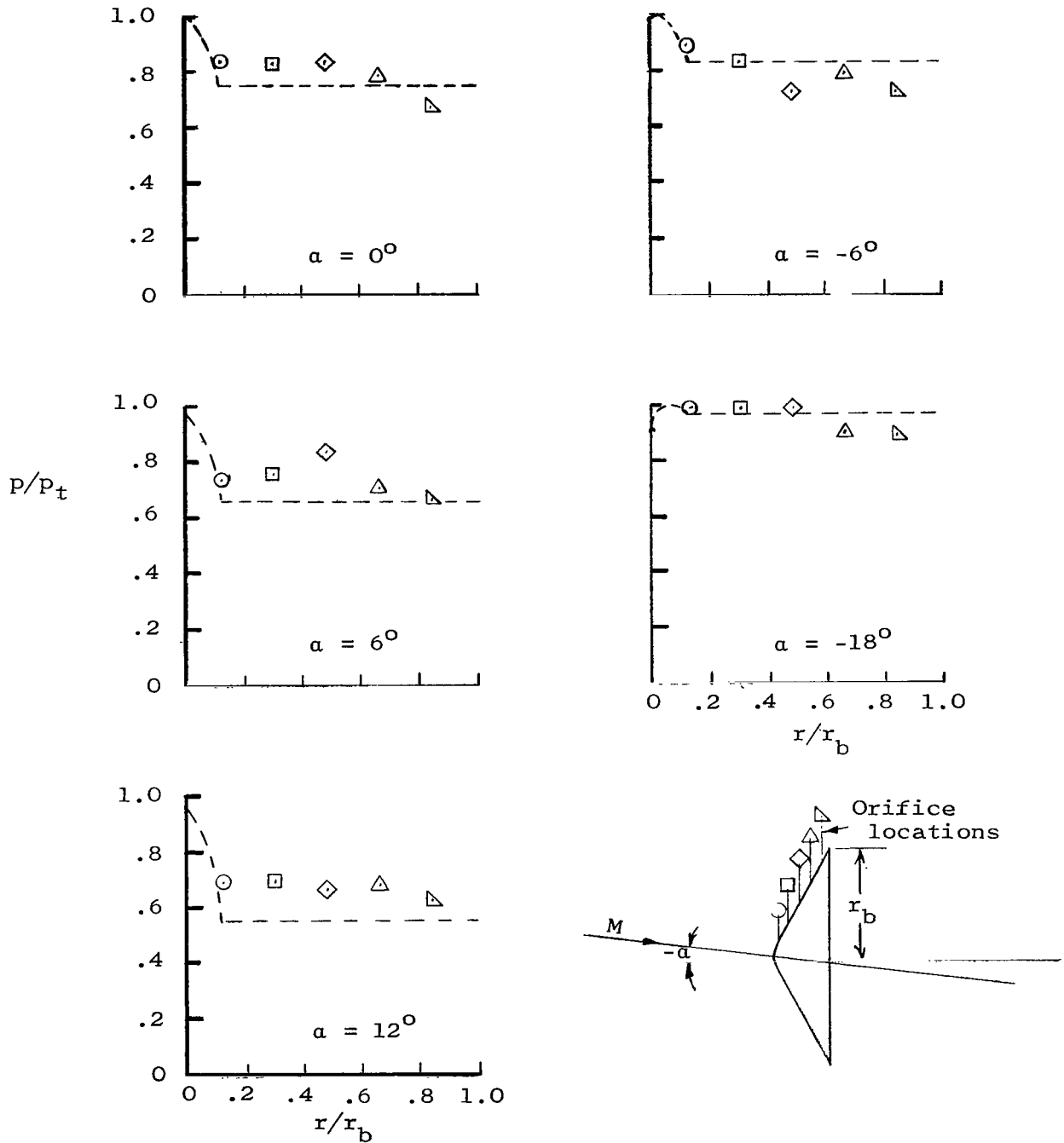r/r_b

Orifice locations

r_b

M

$-\alpha$

Figure 11.- Pressure distribution on a vertical ray of the 120° cone model at several angles of attack.

"The aeronautical and space activities of the United States shall be conducted so as to contribute . . . to the expansion of human knowledge of phenomena in the atmosphere and space. The Administration shall provide for the widest practicable and appropriate dissemination of information concerning its activities and the results thereof."

—NATIONAL AERONAUTICS AND SPACE ACT OF 1958

NASA SCIENTIFIC AND TECHNICAL PUBLICATIONS

TECHNICAL REPORTS: Scientific and technical information considered important, complete, and a lasting contribution to existing knowledge.

TECHNICAL NOTES: Information less broad in scope but nevertheless of importance as a contribution to existing knowledge.

TECHNICAL MEMORANDUMS: Information receiving limited distribution because of preliminary data, security classification, or other reasons.

CONTRACTOR REPORTS: Scientific and technical information generated under a NASA contract or grant and considered an important contribution to existing knowledge.

TECHNICAL TRANSLATIONS: Information published in a foreign language considered to merit NASA distribution in English.

SPECIAL PUBLICATIONS: Information derived from or of value to NASA activities. Publications include conference proceedings, monographs, data compilations, handbooks, sourcebooks, and special bibliographies.

TECHNOLOGY UTILIZATION PUBLICATIONS: Information on technology used by NASA that may be of particular interest in commercial and other non-aerospace applications. Publications include Tech Briefs, Technology Utilization Reports and Notes, and Technology Surveys.

Details on the availability of these publications may be obtained from:

SCIENTIFIC AND TECHNICAL INFORMATION DIVISION

NATIONAL AERONAUTICS AND SPACE ADMINISTRATION

Washington, D.C. 20546